

# Sustainable Smart Tags with Two-Step Verification for Anticounterfeiting Triggered by the Photothermal Response of Upconverting Nanoparticles

Fernando E. Maturi, Carlos D. S. Brites, Robson R. Silva, Karina Nigoghossian, Deivy Wilson, Rute A. S. Ferreira, Sidney J. L. Ribeiro,\* and Luís D. Carlos\*

Quick-response (QR) codes are gaining much consideration in recent years due to their simple and fast readability compared with conventional barcodes. QR codes provide increased storage capacity and safer access to information, fostering the development of optical or printed smart tags as preferred tools for the Internet of Things (IoT). Herein, the combination of  $\text{Yb}^{3+}/\text{Er}^{3+}$ -doped  $\text{NaGdF}_4$  upconverting nanoparticles (UCNPs) with recovered plastic for the fabrication of sustainable screen-printed QR codes is reported. Their photothermal response under distinct power densities of the 980 nm laser irradiation ( $15\text{--}115\text{ W cm}^{-2}$ ) induces color-tuning and temperature sensing. This power dependence is exploited to design a double key molecular keylock accessed by a smartphone camera through the red (R), green (G), and blue (B) (RGB) additive color model and upconversion thermometry. The latter is based on the integrated areas of the  ${}^2\text{H}_{11/2} \rightarrow {}^4\text{I}_{15/2}$  and  ${}^4\text{S}_{3/2} \rightarrow {}^4\text{I}_{15/2}$   $\text{Er}^{3+}$  transitions using the interconnectivity and integration into the IoT network of the mobile phone to download the temperature calibration curve of the UCNPs from a remote server. These findings illustrate the potential of QR codes-bearing UCNPs toward the design of smart tags for mobile optical sensing and anticounterfeiting.

## 1. Introduction

With the ever-growing demand for faster communication methods, higher storage capacity, and improved manufacturing technologies, Industry 4.0 urges to convert passive materials into smart systems to achieve more reliable fabrication routes, easier access to information, unique data identification (ID), and improved anticounterfeiting applications.<sup>[1–3]</sup> In this sense, the use of smart tags is a good choice because they provide a simple way to perform quick read-outs of encrypted information using a smartphone camera in the context of the Internet of Things (IoT).<sup>[4–6]</sup> Quick-response (QR) codes are a gateway to smart tags because they comprise different information in a 2D barcode matrix composed of black and white square modules, greatly improving the amount of stored information using printed materials.<sup>[7]</sup>


In the past years, researchers have been striving to develop novel smart tags based on QR codes to improve the level of encryption and further increase the storage capacity. Several methods were reported,<sup>[8–11]</sup> but the most elegant one is the use of color multiplexing, which relies on the addition of different colors to enhance the storage capacity compared to the common black-white QR codes.<sup>[12]</sup> This approach paves the road for incorporating additional layers of security by using luminescent materials, as optically active components of inks, to produce the QR codes, where hidden information can be accessed upon exposure to specific light sources.<sup>[13,14]</sup> Multiplexed QR codes were shown to display twice the storage capacity of a conventional QR code.<sup>[4,12]</sup> Moreover, luminescent smart QR codes store unique authentication tags that can be securely transmitted to a remote server, enabling trackability and the triggering of security alerts or other additional security features.<sup>[15]</sup>

Among luminescent materials, lanthanide-doped upconverting nanoparticles (UCNPs) can be highlighted due to their efficient conversion of near-infrared (NIR) low-energy radiation in high-energy light emission in the visible spectral range, by a process known as upconversion.<sup>[16–20]</sup> Since UCNPs present singular spectroscopic features such as sharp emission bands, long excited-state lifetimes, and photostable response,<sup>[21]</sup> it is possible to envisage smart tags based on QR codes containing UCNPs that

F. E. Maturi, C. D. S. Brites, R. A. S. Ferreira, L. D. Carlos  
Phantom-g, CICECO – Aveiro Institute of Materials  
Department of Physics  
University of Aveiro  
Aveiro 3810-193, Portugal  
E-mail: lcarlos@ua.pt

F. E. Maturi, R. R. Silva, K. Nigoghossian, S. J. L. Ribeiro  
Institute of Chemistry  
São Paulo State University (UNESP)  
Araraquara, SP 14 800-060, Brazil  
E-mail: sidney.jl.ribeiro@unesp.br

R. R. Silva, D. Wilson  
São Carlos Institute of Physics  
University of São Paulo  
São Carlos, SP 13 566-590, Brazil

 The ORCID identification number(s) for the author(s) of this article can be found under <https://doi.org/10.1002/adpr.202100227>.

© 2021 The Authors. Advanced Photonics Research published by Wiley-VCH GmbH. This is an open access article under the terms of the Creative Commons Attribution License, which permits use, distribution and reproduction in any medium, provided the original work is properly cited.

DOI: 10.1002/adpr.202100227

present a unique luminescent response provided by NIR excitation sources.<sup>[22–27]</sup> Although several luminescent materials display light-emitting properties under ultraviolet (UV) excitation,<sup>[15,28,29]</sup> the use of smart tags containing UCNP provide a step further in anticounterfeiting applications because NIR excitation is more difficult to replicate. Furthermore, NIR irradiation does not give rise to downshifting light emission from conventional luminescent materials, avoiding interference from background luminescence during the readout of the QR code.<sup>[30]</sup> Also, and more exciting, the concomitant controlled heating of the material is an opportunity to explore thermal-dependent features that are not accessible under UV illumination, while transparency is kept.

The use of smart tags containing UCNP is indeed an ingenious strategy because they can be used in the context of “communicating particles,” where a unique color ID and a temperature recorder are integrated into a single platform.<sup>[31]</sup> A major advantage of using UCNP in this context is that different emission colors can be achieved using the power-dependent ratio between different emissions (e.g., the Er<sup>3+</sup> emissions in the red and green spectral regions<sup>[32]</sup>) while the temperature is registered through, for instance, the intensity ratio of the <sup>2</sup>H<sub>11/2</sub>→<sup>4</sup>I<sub>15/2</sub> and <sup>4</sup>S<sub>3/2</sub>→<sup>4</sup>I<sub>15/2</sub> Er<sup>3+</sup> transitions (Yb<sup>3+</sup>/Er<sup>3+</sup> is by far the widely reported pair in Ln<sup>3+</sup>-luminescent thermometry).<sup>[33,34]</sup> Therefore, no further nanoparticle doping is required and both temperature and color information can be retrieved with single wavelength excitation. In addition, this approach paves the way for coupling the temperature sensing and color-tuning properties to QR codes to develop optical sensors that can be read by smartphones, which is an exciting approach for mobile optical (mOptical) sensing.<sup>[35,36]</sup>

Nevertheless, the use of such an advanced strategy for real-world applications only becomes attractive if one may circumvent dispendious fabrication routes of the QR codes, time-consuming data analysis, and complex implementation. In this way, we herein present a novel method to obtain smart tags by serigraph printing using a sustainable strategy to produce optically active inks using polystyrene (PS) recycled from expanded polystyrene (EPS) package wastes through its dissolution into d-limonene, a green solvent extract from orange peel.<sup>[37]</sup> We demonstrate its

applicability to fabricate QR codes embedding NaGdF<sub>4</sub>:Yb<sup>3+</sup>/Er<sup>3+</sup> UCNP and presenting color-tuning and temperature sensing simply by changing the power density of a 980 nm laser excitation source. This power-dependent dual-mode encoding is accessed either through a spectrometer or a smartphone. In the latter, photographs of the QR codes are treated by the red (R), green (G), and blue (B) (RGB) additive color model to access the first codification level of the system. The interconnectivity and integration into the IoT network of the mobile phone allow the download of the temperature calibration curve of the UCNP from a remote server ensuring access to the second encoding level.

## 2. Results and Discussion

### 2.1. PS Recycling

EPS is usually composed of 98% of air, giving rise to low-density solid wastes with an unattractive small-scale collection, uneconomical bulk volume storage, and noncost effective transportation for commercial purposes, which leads to a recycling rate lower than 1%.<sup>[38,39]</sup> As the main commercial form of PS is EPS, it is possible to easily recycle PS by dissolving EPS into organic solvents, therefore, providing a low-energy consumption due to room temperature processability, preventing eventual degradation of PS and allowing solvent recovery afterward.<sup>[40]</sup> The use of d-limonene as solvent is an interesting choice because it can dissolve substantial amounts of EPS (up to 260 g of EPS per liter of d-limonene),<sup>[41]</sup> besides being a biodegradable and low toxicity compound that presents the lowest contribution to global warming among distinct organic solvents.<sup>[37,41,42]</sup> Furthermore, it is a solvent from a renewable source, extracted from orange rinds as a byproduct in orange juice production with a world production of over 70 000 tons per year.<sup>[43]</sup>

To demonstrate the feasibility of using EPS as a reliable source of PS, proton nuclear magnetic resonance (<sup>1</sup>H NMR) spectra were registered for a sample of the EPS used in this work and a reference sample of PS with an average molecular weight of 280 000 g mol<sup>-1</sup> (PS 280 k), presented in **Figure 1**. Both

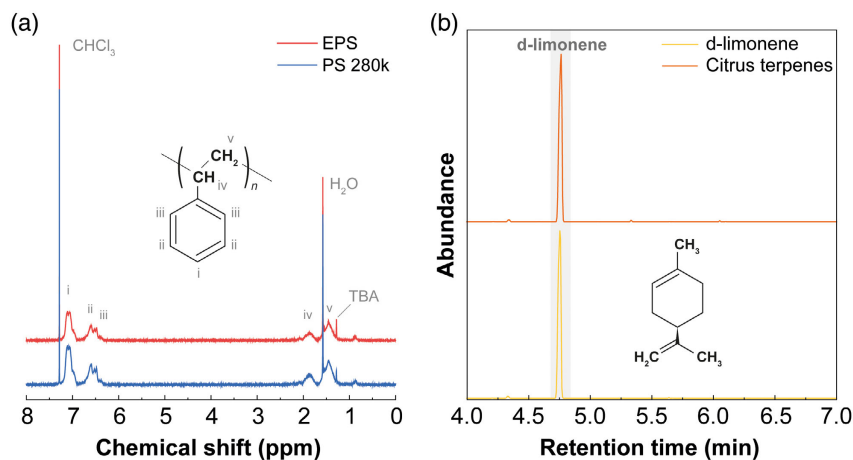


**Figure 1.** a) <sup>1</sup>H NMR spectra of EPS and PS samples (600 MHz, 298 K, CDCl<sub>3</sub>). b) GC–MS chromatogram of d-limonene and citrus terpenes samples. The mass spectrum of the d-limonene found in the citrus terpenes sample is presented in Figure S1, Supporting Information.

samples display the typical chemical shifts ( $\delta$ ) of the aromatic protons of benzene rings between 7.25 and 6.30 ppm (i–iii) and the chemical shifts assigned to CH (iv) and CH<sub>2</sub> (v) at 1.86 and 1.45 ppm, respectively.<sup>[44,45]</sup> Furthermore, residual peaks of *tert*-butyl alcohol (TBA, 1.28 ppm), water (1.60 ppm), and chloroform (7.28 ppm) from impurities in the CDCl<sub>3</sub> solvent are seen.<sup>[46,47]</sup> As there is no structural difference between the samples, EPS can indeed be used as a cheaper and more sustainable source of PS. In addition, reagent grade d-limonene can be replaced by citrus terpenes, which is a high content d-limonene oil obtained through the distillation of the oil extracted from the orange peel. This is supported by the chromatogram of gas chromatography-mass spectrometry (GC-MS) in Figure 1b, where the content of d-limonene (retention time = 4.76 min) is 93% for both citrus terpenes and reagent grade d-limonene. As it is possible to recover PS from EPS wastes by dissolving it in citrus terpenes, these results highlight the feasibility of using renewable solvents to recycle plastics, developing a sustainable approach to fabricate QR codes using low-cost materials and fast printing methods.

## 2.2. UCNPs Characterization and Thermal Response of the QR Codes

NaGdF<sub>4</sub>:Yb<sup>3+</sup>/Er<sup>3+</sup> UCNPs were obtained in a hexagonal plate morphology with a hydrodynamic diameter of 183 ± 72 nm, confirmed by the transmission electron microscopy (TEM) micrograph and dynamic light scattering (DLS) size distribution

presented in **Figure 2**, respectively. The as-synthesized UCNPs display a good dispersion in nonpolar solvents due to the presence of the hydrophobic oleate capping, making them suitable for incorporation into the d-limonene/PS solution to obtain the UCNPs containing PS ink (PS-UCNPs) used to fabricate the QR codes by serigraphy. The screen-printed QR codes present the characteristic Er<sup>3+</sup> upconversion upon 980 nm excitation, with the <sup>2</sup>H<sub>11/2</sub>→<sup>4</sup>I<sub>15/2</sub> (510–534 nm) and <sup>4</sup>S<sub>3/2</sub>→<sup>4</sup>I<sub>15/2</sub> (534–554 nm) transitions of Er<sup>3+</sup> observed in the green spectral range, as shown in **Figure 3**. Moreover, the <sup>2</sup>H<sub>9/2</sub>→<sup>4</sup>I<sub>13/2</sub> originated in the upper energy emitting level of Er<sup>3+</sup> is observed as a shoulder around 555 nm, consistent with recent reports in the literature.<sup>[48,49]</sup>

To record the temperature using the photon upconversion of the obtained QR codes, the ratio between the integrated intensities of the <sup>2</sup>H<sub>11/2</sub>→<sup>4</sup>I<sub>15/2</sub> (*I*<sub>H</sub>) and <sup>4</sup>S<sub>3/2</sub>→<sup>4</sup>I<sub>15/2</sub> (*I*<sub>S</sub>) transitions in the emission spectra shown in Figure 3a was used to define the thermometric parameter  $\Delta = I_H/I_S$  (Experimental Section for details). Further, and as usual in luminescence thermometry,<sup>[50]</sup> the calibration curve  $\Delta(T)$  was acquired (Figure 3b), being *T* the temperature measured with a K-type thermocouple. The thermal sensing ability of the QR codes was evaluated through their relative thermal sensitivity ( $S_r = \frac{1}{\Delta} \left| \frac{\partial \Delta}{\partial T} \right|$ ) and temperature uncertainty ( $\delta T = \frac{1}{S_r} \frac{\partial \Delta}{\Delta}$ ), which are the figures of merit used since 2012 to evaluate the performance of luminescent thermometers.<sup>[33]</sup> The maximum *S<sub>r</sub>* and minimum  $\delta T$  values are

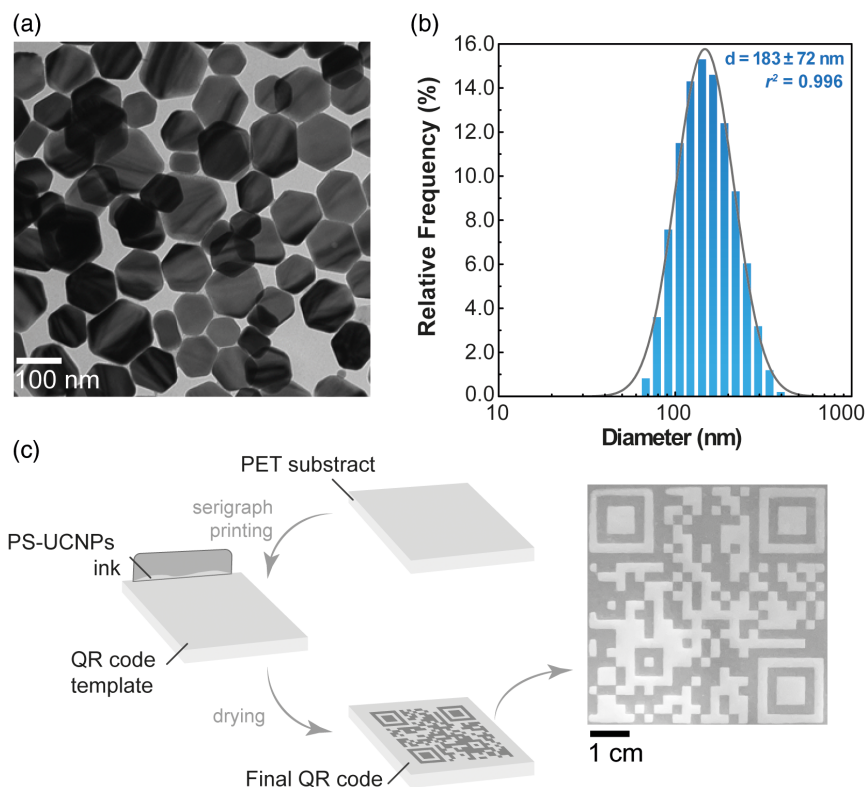


**Figure 2.** a) TEM images and b) hydrodynamic size distribution of the NaGdF<sub>4</sub>:Yb<sup>3+</sup>/Er<sup>3+</sup> UCNPs. The gray line is the best fit to the DLS data using a log-normal distribution ( $r^2 = 0.996$  and fitting parameters shown in Table S1, Supporting Information). c) Schematic representation of the preparation of the QR codes and the final QR code (encoding the URL <http://iq.unesp.br>) under white light illumination.

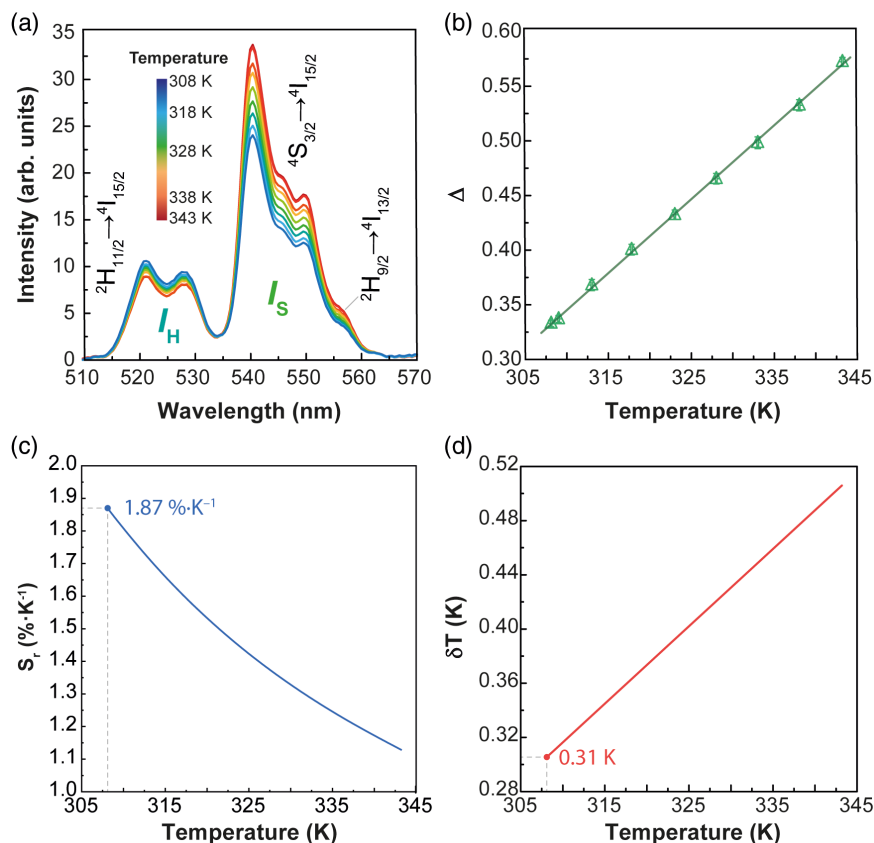


**Figure 3.** a) Temperature-dependent upconversion emission spectra of the QR codes in the 308–343 K range measured at  $P_D = 40 \text{ W cm}^{-2}$ . b)  $\Delta(T)$  calibration curve. The solid line is the best fit to the data using a straight line ( $r^2 > 0.99$ , fitted parameters are shown in Table S2, Supporting Information). c) Relative thermal sensitivity and d) temperature uncertainty of the QR code luminescent thermometer.

1.87 % K<sup>-1</sup> and 0.3 K at 308.0 K, respectively, in good agreement with expected values for NaGdF<sub>4</sub>:Yb<sup>3+</sup>/Er<sup>3+</sup> UCNPs.<sup>[51]</sup> Despite primary luminescent thermometers based on the Boltzmann distribution between the  $^2H_{11/2}$  and  $^4S_{3/2}$  thermally-coupled Er<sup>3+</sup> electronic levels was already demonstrated,<sup>[33]</sup> this approach was not used here because the obtained QR codes absorb light in the spectral region where Boltzmann distribution takes place (Figure S2, Supporting Information). Nevertheless, the thermal calibration indicates that the obtained luminescent QR codes provide accurate temperature readouts from their upconverting emission spectra in the 308–343 K range.

### 2.3. Power-Dependent Dual-Mode Encoding of the QR Codes

The emission of Er<sup>3+</sup> in the red and green spectral regions is strongly affected by the power density ( $P_D$ ) of the excitation source, as already noted in the literature.<sup>[32,52,53]</sup> Indeed,  $I_H$ ,  $I_S$ , and the integrated areas of the  $^2H_{9/2} \rightarrow ^4I_{13/2}$  and  $^4F_{9/2} \rightarrow ^4I_{15/2}$  (635–685 nm) transitions in the QR codes increase with increasing  $P_D$ , following a power law ( $I \propto P_D^n$ , where  $n$  describes the number of photons involved in the upconverting process).<sup>[34]</sup> Therefore,  $n$  corresponds to the slope of the integrated intensities ( $I$ ) versus  $P_D$  in a double-logarithmic plot.<sup>[54]</sup> The values of  $n$  for the four Er<sup>3+</sup> transitions aforementioned are greater than

1.5 (Figure S3, Supporting Information), indicating that the emission in the visible spectral range occurs through a two-photon upconverting process. It is worth pointing out that the contribution of  $^4F_{9/2} \rightarrow ^4I_{15/2}$  transition in the red spectral region is favored at higher  $P_D$  because the  $^2H_{11/2}$  and  $^4S_{3/2}$  upper emitting levels become saturated, favoring the population of the  $^4F_{9/2}$  emitting level due to the higher nonradiative relaxations upon the local heating induced by the laser excitation.<sup>[32,55]</sup> For that reason, the ratio between the integrated intensities of the transitions in the red ( $^4F_{9/2} \rightarrow ^4I_{15/2}$ ) and green ( $^2H_{11/2} \rightarrow ^4I_{15/2}$ ,  $^4S_{3/2} \rightarrow ^4I_{15/2}$ , and  $^2H_{9/2} \rightarrow ^4I_{13/2}$ ) spectral regions, defined as  $\theta$ , increases upon increasing  $P_D$ , resulting in the shift of the emission color from the green to the yellow regions (Figure 4), together with a temperature increase induced by the absorbed photons in the PS substrate and NaGdF<sub>4</sub>:Yb<sup>3+</sup>/Er<sup>3+</sup> UCNPs that are further partially converted into heat. This power-dependent color change gives rise to a simple approach for tuning the emission response of the QR codes without further doping of the obtained UCNPs, allowing easy anticounterfeiting measures based on color matching criteria for the validation of the QR code readout through NIR laser irradiation.

Indeed, it is possible to use the power-dependent upconverting emission spectra of the QR codes upon 980 nm irradiation as input for playing the role of a double key in a molecular keylock.

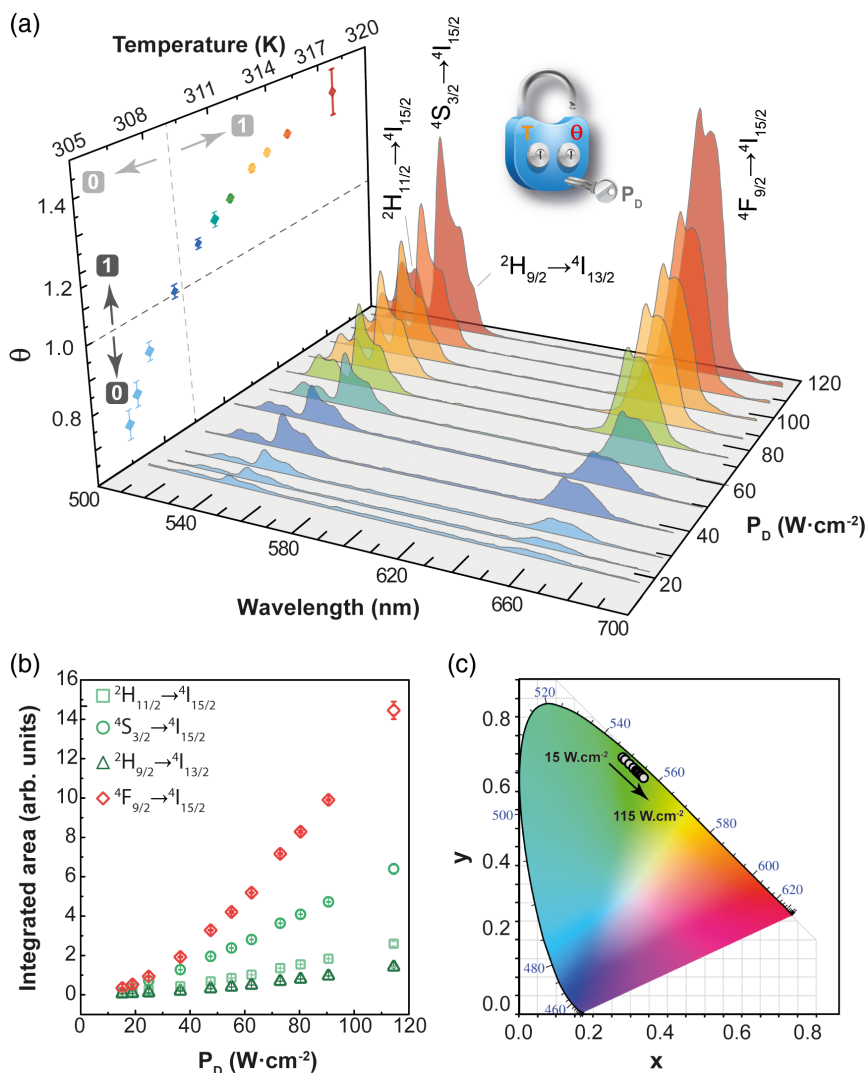


**Figure 4.** a) Upconverting emission spectra of NaGdF<sub>4</sub>:Yb<sup>3+</sup>/Er<sup>3+</sup> UCNPs under excitation at 980 nm varying  $P_D$ . The intensity ratio  $\theta$  between the integrated intensities of the transitions in the red ( $^4F_{9/2} \rightarrow ^4I_{15/2}$ ) and green ( $^2H_{11/2} \rightarrow ^4I_{15/2}$ ,  $^4S_{3/2} \rightarrow ^4I_{15/2}$ , and  $^2H_{9/2} \rightarrow ^4I_{13/2}$ ) spectral regions is presented in the inset. The keylock represents the dual encoding of the QR code emission (unlocked by  $P_D$  values) enabling a two-step verification using temperature ( $T$ ) and  $\theta$ . b) Integrated emission intensities of the  $^2H_{11/2} \rightarrow ^4I_{15/2}$ ,  $^4S_{3/2} \rightarrow ^4I_{15/2}$ ,  $^2H_{9/2} \rightarrow ^4I_{13/2}$ , and  $^4F_{9/2} \rightarrow ^4I_{15/2}$  transitions. c) CIE 1931 chromaticity diagram coordinates of the QR code at different  $P_D$  values.

The  $P_D$  physical input triggers simultaneously color and temperature changes. Therefore, by setting a threshold for  $\theta = 1.0$  (same intensities in the red and green spectral regions, corresponding to a  $P_D = 40 \text{ W cm}^{-2}$ ), we can design the first encoding level of the system. Whenever this first  $\theta$ -key opens the system, we can go further to the second level of encoding determining the absolute temperature for  $P_D > 40 \text{ W cm}^{-2}$  with the calibration curve described in Section 2.2. The threshold to open the system with this temperature key ( $T$ -key) is  $T = 309 \text{ K}$ , the temperature corresponding to  $\theta = 1$  (Figure 4a). It is important to point out that despite the calibration curve was only recorded at  $P_D = 40 \text{ W cm}^{-2}$ , it is still possible to extrapolate its use to different  $P_D$  because there is a good agreement between the temperature calculated with the calibration curve and the temperature measured with a thermocouple.

#### 2.4. Molecular Keylock Through RGB Color Space Readout

Figure 5 shows the color variation of the photographs of the luminescent QR codes under different  $P_D$  taken with a smartphone camera. Each image is composed of an RGB additive color model, creating the color through the mix of red (R), green (G), and blue (B) primary colors (Figure S4, Supporting Information). The changes in the emission color of the QR codes observed in Figure 5b are assessed by the ratio of intensities of the R and G color channels (R/G), similarly to what we describe for the  $\theta$  parameter shown in Figure 4a. As expected, the intensity of all color channels increases when increasing  $P_D$ , with the R and G channels playing a major role in the composition of the color emission of the QR codes (Figure 5c). The intensity of the B channel is detected during the decomposition of the photographs

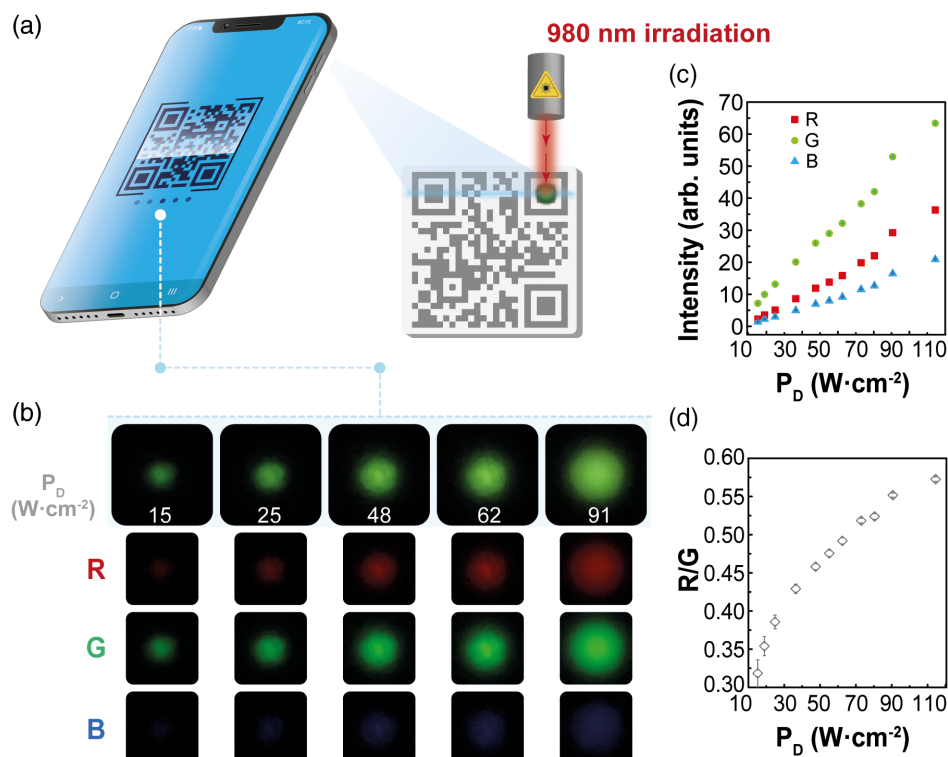


**Figure 5.** a) Scheme of the simultaneous QR code readout and image acquisition. b) Power-dependent photographs of the QR codes upon 980 nm irradiation and the corresponding color channels. c) Integrated intensities of the red, green, and blue color channels. d) Evolution of the red-to-green ratio upon power density increasing.

due to the  ${}^2\text{H}_{9/2} \rightarrow {}^4\text{I}_{15/2}$  emission in the blue spectral region (Figure S4, Supporting Information), despite being too faint to be perceived by naked eyes.

Nevertheless, as the R and G channels cover almost the spectral regions of the  ${}^4\text{F}_{9/2} \rightarrow {}^4\text{I}_{15/2}$  and  ${}^2\text{H}_{11/2} \rightarrow {}^4\text{I}_{15/2}/{}^4\text{S}_{3/2} \rightarrow {}^4\text{I}_{15/2}/{}^2\text{H}_{9/2} \rightarrow {}^4\text{I}_{13/2}$  transitions, respectively, the ratiometric response of the R and G channels obtained from the images of the QR codes at distinct  $P_D$  (Figure 5d) presents the same power-dependent profile observed for the ratiometric  $\theta$  curve shown in Figure 4a. In addition to the same profile, both cases show the same twofold improvement in the ratiometric evolution when increasing  $P_D$  from 15 to 115  $\text{W cm}^{-2}$  (Figure S5, Supporting Information). Therefore, the first codification level of the system can be accessed by the smartphone readout of the photographs of the luminescent QR codes setting  $R/G = 0.43$  as the threshold, equivalent to  $\theta = 1.0$ . Direct access to the second encoding level is not possible based only on the photographs because the RGB additive color model does not permit the determination of the temperature. This apparent limitation is, however, overcome by the integration of the smartphone into the IoT network allowing the download of the calibration curve of these UCNP from a remote server, since the temperature dependence of  $\theta$  can be extrapolated to the temperature dependence of  $R/G$  (Figure S5, Supporting Information). This permits a faster and user-friendly  $T$ -key decryption route, without jeopardizing the  $\theta$ -key access. Moreover, the direct decoding of the  $T$ -key only by spectral measurements results in different

access privileges to distinct readout methodologies, a feature that is an added benefit of the reported methodology.

### 3. Conclusions

The preparation through a facile sustainable route of screen-printed luminescent QR codes acting as two-step encoding smart tags was demonstrated. Luminescent inks were obtained by recycling PS from EPS wastes, using d-limonene as a green solvent, and incorporating  $\text{NaGdF}_4:\text{Yb}^{3+}/\text{Er}^{3+}$  UCNP in the obtained PS/d-limonene solution. QR codes were fabricated through a low-cost printing method (serigraph printing in this case, however, inked or spaying could be also used). Taking advantage of the radiation-to-heat conversion of the UCNP-bearing QR codes under 980 nm irradiation, we exploited their power-dependent emission, and the corresponding temperature increase, to create a double key molecular keylock accessible either through spectral features or the RGB additive color model. Setting the irradiation power density to 40  $\text{W cm}^{-2}$ , and adopting threshold values  $\theta = 1.0$  or  $R/G = 0.43$ , we designed the color encoding level of the system (first level) that is accessed both by a spectrometer or a smartphone. Then, the temperature encoding level (second level) is implemented based on the integrated areas of the  ${}^2\text{H}_{11/2} \rightarrow {}^4\text{I}_{15/2}$  and  ${}^4\text{S}_{3/2} \rightarrow {}^4\text{I}_{15/2}$  transitions in the green spectral range that enable the absolute temperature determination. Direct access to this second encoding level is not possible based on the photographs of the QR codes. This apparent limitation is, however,

overcome using one of the main advantages of smartphones: their interconnectivity and integration into the IoT network that allows the real-time download of the calibration curve of the  $\text{NaGdF}_4:\text{Yb}^{3+}/\text{Er}^{3+}$  UCNP from a remote server. The impossibility to directly decode one level of a system by a specific technology results in different access privileges to distinct readouts. This approach can be easily generalized to other UCNP and is a step toward the design of smart-tags for anti-counterfeiting.

## 4. Experimental Section

**Materials:** Gadolinium oxide ( $\text{Gd}_2\text{O}_3$ ), ytterbium oxide ( $\text{Yb}_2\text{O}_3$ ), erbium oxide ( $\text{Er}_2\text{O}_3$ ), trifluoroacetic acid ( $\text{CF}_3\text{CO}_2\text{H}$ ), sodium trifluoroacetate ( $\text{CF}_3\text{CO}_2\text{Na}$ ), oleic acid, 1-octadecene, silicon dioxide ( $\text{SiO}_2$ ) nanopowder (10–20 nm particle size), (R)-(+)-limonene (d-limonene), and PS with average molecular weight of  $280\,000\text{ g mol}^{-1}$  (PS 280 k) were purchased from Sigma-Aldrich. Citrus terpenes were supplied by Citrosuco S/A (Matão, Brazil). EPS were obtained from packaging materials and used as a source of PS.

**Synthesis of  $\text{Yb}^{3+}/\text{Er}^{3+}$  Codoped  $\text{NaGdF}_4$  Upconverting Nanoparticles:** The UCNP were prepared through the thermal decomposition of sodium and lanthanide trifluoroacetates into  $\text{NaGdF}_4:\text{Yb}^{3+}/\text{Er}^{3+}$  following a previously reported method with minor modifications.<sup>[56]</sup> First, the lanthanide trifluoroacetate precursor was prepared by reacting  $\text{Gd}_2\text{O}_3$  (353.4 mg, 0.975 mmol),  $\text{Yb}_2\text{O}_3$  (98.5 mg, 0.250 mmol), and  $\text{Er}_2\text{O}_3$  (9.6 mg, 0.025 mmol) with  $\text{CF}_3\text{CO}_2\text{H}$  in a mixture with water (1:1, 10 mL) in a 50 mL three-neck round bottom flask (molar ratio of Gd:Yb:Er = 78:20:2). The mixture was refluxed at 353 K for 12 h. After obtaining a clear solution, the temperature was lowered to 333 K, and the flask was opened to evaporate the solvents and get the precursor powder. The second step consists of adding 340 mg of  $\text{CF}_3\text{CO}_2\text{Na}$  and 7.5 mL each of oleic acid and 1-octadecene to the flask. In a second three-neck round bottom flask (100 mL), 12.5 mL each of oleic acid and 1-octadecene were added. The flasks were connected to a Schlenk line to remove moisture and oxygen for 30 min at 398 K under vacuum and magnetic stirring. Subsequently, the flask containing oleic acid and 1-octadecene was heated to 593 K under argon flow at a heating rate of  $10\text{ K min}^{-1}$ . The precursor solution kept at 398 K was then collected with a glass syringe and injected into the second flask (injection rate of  $1.5\text{ mL min}^{-1}$  controlled by a pump system). The temperature was kept at 583 K for 90 min under stirring and argon flow. After cooling down to room temperature, the nanoparticles were precipitated by addition of ethanol and collected by centrifugation at 5350 RCF for 10 min. The nanoparticles were redispersed in hexane and washed twice with ethanol (1:5 v/v). The oleate capped  $\text{NaGdF}_4:\text{Yb}^{3+}/\text{Er}^{3+}$  nanoparticles were finally redispersed in hexane for further use.

**Preparation of Luminescent Ink:** A clear and viscous solution was obtained by dissolving EPS (2.0 g) in citrus terpenes (5.0 mL), followed by its centrifugation at 7500 rpm to remove particulate material from the packaging used as the source of EPS. The UCNP containing PS inks (PS-UCNP) were prepared through the addition of 30 wt%  $\text{SiO}_2$  nanopowder as a thickening agent and 0.1 wt% of UCNP into the previously prepared solution and then mixing them in a SpeedMixer (DAC150.1 FVZ-K, FlackTek) by 2 min at 2000 rpm.

**Fabrication of Luminescent QR Codes by Serigraph Printing:** A QR code template ( $6 \times 6\text{ cm}^2$ ) linking to the website of the Institute of Chemistry, UNESP (<http://iq.unesp.br/>) was fabricated in a 150-mesh polyester screen to print the luminescent QR codes using an automatic press (IMAH, Paraná, Brazil) through a press-printing method (serigraph printing). The previously prepared luminescent ink was cast onto the polyester screen containing the QR code template and then pressed against the screen to print the luminescent QR codes onto polyethylene terephthalate (PET) substrates. This method allowed for printing ten individual codes per minute using 10 mL of luminescent ink. Three different (and

illustrative) QR codes obtained through this methodology are shown in Figure S6, Supporting Information.

**Transmission Electron Microscopy:** The morphological structure and size of the UCNP were analyzed from TEM images acquired in an electron microscope (Tecnai G2 Spirit BioTwin, FEI) operating at 120 kV.

**Dynamic Light Scattering:** The hydrodynamic size (diameter,  $d$ ) of the UCNP was measured by DLS in a Zetasizer Nano ZS instrument (ZEN3600, Malvern) operating with a 632.8 nm He–Ne laser at 298 K. The UCNP samples dispersed in hexane were measured with a dip cell kit (ZEN1002, Malvern) coupled to a square glass cell (PCS1115, Malvern) by performing three measurements with ten scans each, where the average value is reported in Figure 2b.

**Proton Nuclear Magnetic Resonance:** The  $^1\text{H}$  NMR spectra of EPS and PS were acquired in a 600 MHz Bruker Avance III spectrometer (HD 600, Bruker) operating at 14.1 T. Samples were dissolved in deuterated chloroform ( $\text{CDCl}_3$ ,  $8\text{ mg mL}^{-1}$ ) and the spectra were registered at 298 K in the manual mode. Automated tuning, locking, shimming, and calibration of  $90^\circ$  pulses were performed using standard Bruker routines.

**Gas Chromatography–Mass Spectrometry:** The GC–MS analysis was used to determine the content of d-limonene in standard and citrus terpenes samples. The analysis was carried out in a gas chromatography equipment (7890B, Agilent) coupled to a mass spectrometer (5977 A, Agilent) using a capillary column with a stationary phase of (5%-phenyl)-methylpolysiloxane (30 m length  $\times$  0.25 mm inner diameter, HP5-MS Agilent) with electron impact ionization at 70 eV, helium as the carrier gas (flow rate =  $1\text{ mL min}^{-1}$ ) and a split ratio of 100:1. The GC–MS temperature program was as follows: 353 K for 3 min, then ramp to 553 K at  $30\text{ K min}^{-1}$ , then hold 10 min. The samples were prepared by diluting d-limonene and citrus terpene in ethyl acetate (HPLC grade,  $1\text{ mg mL}^{-1}$ ).

**Photoluminescence Spectroscopy:** The emission spectra of the luminescent QR codes were recorded in the experimental setup shown in Figure S7, Supporting Information. The excitation of the sample was carried out at  $980 \pm 10\text{ nm}$  with a collimated fiber-coupled continuous-wave (CW) laser system (MDL-980-FC-10 W, CNI). The emission spectra were registered by a USB-portable spectrometer (Maya 2000 Pro, Ocean Optics) coupled to an optical fiber (QP450-1-XSR, Ocean Optics) using an edge pass filter (FESH0750, Thorlabs) to cut off the excitation signal during the spectral acquisition (100 spectra were recorded for each temperature and  $P_D$  using an integration time of 250 ms).

**Thermal Calibration:** The temperature-dependent measurements were performed attaching a homemade Peltier temperature controller (0.1 K resolution) to the abovementioned experimental setup. The calibration of temperature was performed by placing a K-type thermocouple with a temperature uncertainty of 0.1 K (KA01-3, TME Thermometers) coupled to a thermocouple data logger (TC-08, Pico Technology) onto the surface of the QR code, 0.5 cm away from the laser spot to avoid heating the thermocouple with the beam spot.

**Calculation of the Integrated Areas:** The areas corresponding to the  $\text{Er}^{3+}$   $^2\text{H}_{11/2} \rightarrow ^4\text{I}_{15/2}$ ,  $^4\text{S}_{3/2} \rightarrow ^4\text{I}_{15/2}$ ,  $^2\text{H}_{9/2} \rightarrow ^4\text{I}_{13/2}$ , and  $^4\text{F}_{9/2} \rightarrow ^4\text{I}_{15/2}$  transitions were obtained through the deconvolution of the emission spectra of the QR codes using a custom code written in MATLAB 2021a under the license provided to the University of Aveiro. First, each emission spectrum was converted from wavelength to energy units using the Jacobian conversion.<sup>[57]</sup> Good fits ( $r^2 > 0.99$ ) were obtained by adjusting 11 Gaussian functions to the experimental data, as presented in Figure S8, Supporting Information. The reported areas and errors are the average and standard deviation values from 100 spectra measured per temperature or  $P_D$ . The integrated emission of  $^2\text{H}_{11/2} \rightarrow ^4\text{I}_{15/2}$  and  $^4\text{S}_{3/2} \rightarrow ^4\text{I}_{15/2}$  transitions correspond to the sum of the areas of their respective Gaussian functions. The integrated emission of the red spectral region is the sum of the areas corresponding to the  $^4\text{F}_{9/2} \rightarrow ^4\text{I}_{15/2}$  transition while the integrated emission of the green spectral region is the sum of the areas of the Gaussian functions corresponding to the  $^2\text{H}_{11/2} \rightarrow ^4\text{I}_{15/2}$ ,  $^4\text{S}_{3/2} \rightarrow ^4\text{I}_{15/2}$ , and  $^2\text{H}_{9/2} \rightarrow ^4\text{I}_{13/2}$  transitions.

**Power Density Determination:** The CW laser power and the corresponding beam profile were measured with a power meter (FieldMaxII – TOPOP – 2 Vis, Coherent) and a charge-coupled device (CCD) camera (BC106N – VIS/M, Thorlabs) coupled to a neutral density

filter (NE50B-B, Thorlabs), respectively. The resulting beam profile intensity was obtained for each laser power by averaging the intensity of ten sequential scans. The beam profile intensity values were calibrated to power density considering that the integrated area of the beam profile is the laser power (in W) measured with the power meter. Therefore, the average laser power density was calculated considering the values above 13.5% ( $1/e^2$ , the cut-off value for Gaussian beams). The beam cross-section at  $1/e^2$  is displayed in Figure S9, Supporting Information.

**Image Acquisition:** Photographs of the luminescent QR codes under 980 nm irradiation were taken with a smartphone camera (iPhone 12, Apple) with a resolution of  $3024 \times 4032$  pixel<sup>2</sup>, aperture of  $f/1.6$ , and a sensor dimension of  $1/3.6''$ . Images were acquired using the commercially available Camera+ 2 app to ensure the same lighting conditions during the experiment, setting the shutter speed to  $1/45$  s and locked ISO 1000 to avoid pixel saturation from the bright light emission from the QR codes under 980 nm exposure.

**Image Processing:** The RGB color model was used to evaluate the changes in the emission color of the QR codes upon increasing laser power density. A custom MATLAB 2021a code was designed to analyze the ratio between the intensity of the red and green channels ( $R/G$ ). The code imports the power-dependent pictures of the QR codes cropping them in a  $251 \times 251$  pixel<sup>2</sup> region centered in the laser spot. Each cropped image was split into three-color channels: red ( $R$ ), green ( $G$ ), and blue ( $B$ ). The intensity profiles reported to each channel along the orthogonal directions correspond to the line and column integration of the intensities. The reported integrated intensities values correspond to the total integrated intensities of each channel. The corresponding uncertainties were obtained by multiplying the integrated intensity by the inverse signal-to-noise ratio retrieved from the intensity profiles in the two orthogonal directions. The red-to-green ratio ( $R/G$ ) is finally calculated as the ratio between the integrated intensities of the  $R$  and  $G$  channels. Detailed information on the image processing procedure is given in Section S1.4, Supporting Information.

## Supporting Information

Supporting Information is available from the Wiley Online Library or from the author.

## Acknowledgements

This work was developed within the scope of the projects CICECO-Aveiro Institute of Materials (UIDB/50011/2020 and UIDP/50011/2020) and Shape of Water (PTDC/NAN-PRO/3881/2020) financed by Portuguese funds through the FCT/MEC and when appropriate cofinanced by FEDER under the PT2020 Partnership Agreement. F.E.M. acknowledges the funding received from the European Union's Horizon 2020 research and innovation programme under the Marie Skłodowska-Curie grant agreement no. 823941. The support of the European Union's Horizon 2020 FET Open program under grant agreement no. 801305 (NanoTBTech) is also acknowledged. R.R.S. acknowledges the financial support from the Brazilian agency FAPESP (process no. 16/06612-6).

## Conflict of Interest

The authors declare no conflict of interest.

## Data Availability Statement

Research data are not shared.

## Keywords

anticounterfeiting, luminescence thermometry, quick-response codes, two-step verification, upconverting nanoparticles

Received: July 30, 2021

Revised: October 5, 2021

Published online: December 21, 2021

- [1] B. Tjahjono, C. Esplugues, E. Ares, G. Pelaez, *Procedia Manuf.* **2017**, *13*, 1175.
- [2] E. Sisinni, A. Saifullah, S. Han, U. Jennehag, M. Gidlund, *IEEE Trans. Ind. Informatics* **2018**, *14*, 4724.
- [3] R. A. Khalil, N. Saeed, M. Masood, Y. M. Fard, M.-S. Alouini, T. Y. Al-Naffouri, *IEEE Internet Things J.* **2021**, *8*, 11016.
- [4] J. F. C. B. Ramalho, S. F. H. Correia, L. Fu, L. L. F. António, C. D. S. Brites, P. S. André, R. A. S. Ferreira, L. D. Carlos, *Adv. Sci.* **2019**, *6*, 1900950.
- [5] H. Elazhary, *J. Netw. Comput. Appl.* **2019**, *128*, 105.
- [6] G. Aceto, V. Persico, A. Pescapé, *J. Ind. Inf. Integr.* **2020**, *18*, 100129.
- [7] J. F. C. B. Ramalho, L. C. F. António, S. F. H. Correia, L. S. Fu, A. S. Pinho, C. D. S. Brites, L. D. Carlos, P. S. André, R. A. S. Ferreira, *Opt. Laser Technol.* **2018**, *101*, 304.
- [8] N. Victor, *Int. J. Comput. Appl.* **2012**, *60*, 17.
- [9] M. M. Umaria, G. B. Jethava, in *Int. Conf. Comput. Intell. Commun. Networks*, IEEE, Piscataway, NJ **2015**, pp. 1094–1096.
- [10] A. Abas, Y. Yusof, R. Din, F. Azali, B. Osman, *Bull. Electr. Eng. Informatics* **2020**, *9*, 2555.
- [11] J. Chiang, C. Hsia, H. Li, *Electron. Lett.* **2013**, *49*, 1381.
- [12] P. S. André, R. A. S. Ferreira, *Electron. Lett.* **2014**, *50*, 1828.
- [13] L. Yang, Z. Wang, S. Fan, J. Feng, Y. Zhong, T. Zhao, Y. Hu, Y. Liu, *Nanosci. Nanotechnol. Lett.* **2019**, *11*, 451.
- [14] F. Miller, S. Wintzheimer, J. Prieschl, V. Strauss, K. Mandel, *Adv. Opt. Mater.* **2021**, *9*, 2001972.
- [15] J. F. C. B. Ramalho, S. F. H. Correia, L. Fu, L. M. S. Dias, P. Adão, P. Mateus, R. A. S. Ferreira, P. S. André, *NPJ Flex. Electron.* **2020**, *4*, 11.
- [16] F. Auzel, *Chem. Rev.* **2004**, *104*, 139.
- [17] F. Wang, Y. Han, C. S. Lim, Y. Lu, J. Wang, J. Xu, H. Chen, C. Zhang, M. Hong, X. Liu, *Nature* **2010**, *463*, 1061.
- [18] M. Haase, H. Schäfer, *Angew. Chem. Int. Ed.* **2011**, *50*, 5808.
- [19] J. Zhou, Q. Liu, W. Feng, Y. Sun, F. Li, *Chem. Rev.* **2015**, *115*, 395.
- [20] M. Bettinelli, L. Carlos, X. Liu, *Phys. Today* **2015**, *68*, 38.
- [21] J.-C. Boyer, F. Vetrone, L. A. Cuccia, J. A. Capobianco, *J. Am. Chem. Soc.* **2006**, *128*, 7444.
- [22] N. M. Sangeetha, P. Moutet, D. Lagarde, G. Sallen, B. Urbaszek, X. Marie, G. Viau, L. Ressler, *Nanoscale* **2013**, *5*, 9587.
- [23] M. You, J. Zhong, Y. Hong, Z. Duan, M. Lin, F. Xu, *Nanoscale* **2015**, *7*, 4423.
- [24] M. You, M. Lin, S. Wang, X. Wang, G. Zhang, Y. Hong, Y. Dong, G. Jin, F. Xu, *Nanoscale* **2016**, *8*, 10096.
- [25] W. Yao, Q. Tian, J. Liu, Q. Xue, M. Li, L. Liu, Q. Lu, W. Wu, *Nanoscale* **2017**, *9*, 15982.
- [26] G. Gong, Y. Song, H. Tan, S. Xie, C. Zhang, L. Xu, J. Xu, J. Zheng, *Compos. Part B Eng.* **2019**, *179*, 107504.
- [27] F. Kholi, N. Ghazyani, M. Riahi, H. Zare-Behtash, M. H. Majles Ara, E. Heydari, *ACS Appl. Nano Mater.* **2019**, *2*, 3590.
- [28] Y. Ma, Y. Dong, S. Liu, P. She, J. Lu, S. Liu, W. Huang, Q. Zhao, *Adv. Opt. Mater.* **2020**, *8*, 1901687.
- [29] N. Katumo, L. A. Ruiz-Preciado, V. Kumar, G. Hernandez-Sosa, B. S. Richards, I. A. Howard, *Adv. Mater. Technol.* **2021**, *6*, 2100047.
- [30] J. M. Meruga, W. M. Cross, P. Stanley May, Q. Luu, G. A. Crawford, J. J. Kellar, *Nanotechnology* **2012**, *23*, 395201.



- [31] J. Reichstein, F. Miller, S. Wintzheimer, K. Mandel, *Adv. Funct. Mater.* **2021**, 2104189, 2104189.
- [32] M. Kraft, C. Würth, V. Muhr, T. Hirsch, U. Resch-Genger, *Nano Res.* **2018**, 11, 6360.
- [33] C. D. S. Brites, S. Balabhadra, L. D. Carlos, *Adv. Opt. Mater.* **2019**, 7, 1801239.
- [34] C. D. S. Brites, S. V. Kuznetsov, V. A. Konyushkin, A. N. Nakladov, P. P. Fedorov, L. D. Carlos, *Eur. J. Inorg. Chem.* **2020**, 2020, 1555.
- [35] N. Katumo, G. Gao, F. Laufer, B. S. Richards, I. A. Howard, *Adv. Opt. Mater.* **2020**, 8, 2000507.
- [36] J. F. C. B. Ramalho, L. D. Carlos, P. S. André, R. A. S. Ferreira, *Adv. Photonics Res.* **2021**, 2, 2000211.
- [37] R. Ciriminna, M. Lomeli-Rodríguez, P. D. Carà, J. A. Lopez-Sanchez, M. Pagliaro, P. Demma Carà, J. A. Lopez-Sanchez, M. Pagliaro, *Chem. Commun.* **2014**, 50, 15288.
- [38] M. D. Samper, D. Garcia-Sanoguera, F. Parres, J. López, *Prog. Rubber Plast. Recycl. Technol.* **2010**, 26, 83.
- [39] EPA, *Plastics*, **2015** <https://archive.epa.gov/epawaste/conservation/tools/warm/pdfs/Plastics.pdf> (accessed: March 2015).
- [40] Y.-B. Zhao, X.-D. Lv, H.-G. Ni, *Chemosphere* **2018**, 209, 707.
- [41] M. T. García, I. Gracia, G. Duque, A. de Lucas, J. F. Rodríguez, *Waste Manag.* **2009**, 29, 1814.
- [42] G. Paggiola, S. Van Stempvoort, J. Bustamante, J. M. V. Barbero, A. J. Hunt, J. H. Clark, *Biofuels Bioprod. Biorefining* **2016**, 10, 686.
- [43] M. Firdaus, L. M. de Espinosa, M. A. R. Meier, *Macromolecules* **2011**, 44, 7253.
- [44] J. Zhang, H. Huang, Y. Guan, D.-F. Wei, F.-Z. Hu, A.-N. Zheng, H.-N. Xiao, *J. Appl. Polym. Sci.* **2010**, 117, 2566.
- [45] J. W. Wackerly, J. F. Dunne, *J. Chem. Educ.* **2017**, 94, 1790.
- [46] H. E. Gottlieb, V. Kotlyar, A. Nudelman, *J. Org. Chem.* **1997**, 62, 7512.
- [47] G. R. Fulmer, A. J. M. Miller, N. H. Sherden, H. E. Gottlieb, A. Nudelman, B. M. Stoltz, J. E. Bercaw, K. I. Goldberg, *Organometallics* **2010**, 29, 2176.
- [48] J. C. Martins, A. R. N. Bastos, R. A. S. Ferreira, X. Wang, G. Chen, L. D. Carlos, *Adv. Photonics Res.* **2021**, 2, 2000169.
- [49] T. P. Van Swieten, T. Van Omme, D. J. van den Heuvel, S. J. W. Vonk, R. G. Spruit, F. Meirer, H. H. P. Garza, B. M. Weckhuysen, A. Meijerink, F. T. Rabouw, R. G. Geitenbeek, *ACS Appl. Nano Mater.* **2021**, 4, 4208.
- [50] C. D. S. Brites, A. Millán, L. D. Carlos, in *Handb. Phys. Chem. Rare Earths*, (Eds: B. Jean-Claude, P. Vitalij K.), Elsevier, Amsterdam, **2016**, 339–427.
- [51] K. Nigoghossian, Y. Messaddeq, D. Boudreau, S. J. L. Ribeiro, *ACS Omega* **2017**, 2, 2065.
- [52] X. Zhang, Z. Zhang, Z. Liu, C. Zhang, B. Zhang, X. Mi, H. Zheng, *J. Lumin.* **2019**, 205, 374.
- [53] H. Bae, E. Lee, K. T. Lee, *Phys. Chem. Chem. Phys.* **2021**, 23, 14587.
- [54] M. Pollnau, D. R. Gamelin, S. R. Lüthi, H. U. Güdel, M. P. Hehlen, *Phys. Rev. B* **2000**, 61, 3337.
- [55] J. F. Suyver, A. Aebischer, S. García-Revilla, P. Gerner, H. U. Güdel, *Phys. Rev. B* **2005**, 71, 125123.
- [56] E. Hemmer, M. Quintanilla, F. Légaré, F. Vetrone, *Chem. Mater.* **2015**, 27, 235.
- [57] J. Mooney, P. Kambhampati, *J. Phys. Chem. Lett.* **2013**, 4, 3316.